

Cite this article as: Li Tong, Shen Houfa. Multicomponent Modeling of Freckle Formation in IN718 Superalloy During Horizontal Directional Solidification and Vacuum Arc Remelting[J]. Rare Metal Materials and Engineering, 2022, 51(11): 4076-4084.

ARTICLE

Multicomponent Modeling of Freckle Formation in IN718 Superalloy During Horizontal Directional Solidification and Vacuum Arc Remelting

Li Tong, Shen Houfa

School of Materials Science and Engineering, Tsinghua University, Beijing 100084, China

Abstract: A multicomponent two-phase model was established to describe the macro/micro-transportation and the freckle formation during solidification, and the dynamic mesh algorithm was applied to perform the filling process during the vacuum arc remelting (VAR). Firstly, the thermodynamic calculation approach was used to evaluate the liquid composition with the variation of solid fraction during solidification, and the interdendritic liquid density of multicomponent alloys was obtained. Then, the freckle formed during the horizontal directional solidification was simulated and compared with the experiment one to study the freckle formation mechanism and influence factor. Finally, the developed model was used to investigate the influence of process parameters on the freckle formation in the industrial-scale VAR casting. Results show that the element composition has a significant effect on the density change of liquid phase during the solidification. The freckle forms with a high thermosolutal convection strength. The growth direction of freckles is determined by the liquid density difference and the angle between solidified interface and gravity direction. It is also found that the molten pool profile is affected by the electrode melting rate and cooling rate during VAR.

Key words: freckle; macrosegregation; numerical simulation; superalloys; vacuum arc remelting

Superalloys are widely used in critical components, such as aero-engines, aerospace gas turbines, and other high temperature parts^[1-4], which require high yield strength, excellent fatigue resistance, and uniform structure. The various elements in superalloys play an important role in improving the material performance, but they are prone to the formation of freckles, macrosegregation, and other defects. Vacuum arc remelting (VAR) is a smelting process for superalloys, which can remove the inclusions and improve the purity of ingots. However, the freckles cannot be removed once they appear, thereby causing irreversible damage to the products and resulting in the unacceptable loss^[5].

The freckles are considered as the macrosegregation defects caused by the flow of solute-rich interdendritic liquid in the mushy zone during the solidification process, which is related to the shape of mushy zone and the density of liquid phase. Based on the metallurgical morphology, it is generally believed that the freckles are a type of channel segregation.

Copley et al^[6] conducted the directional solidification of NH_4Cl and observed the formation process of in-situ vertical channels. Sarazin^[7] and Sample^[8] et al also observed the similar phenomena for the directional solidification of Pb-Sn-Sb alloy system and proposed a channel formation mechanism based on the density difference for convection. Felicelli et al^[9,10] used the numerical methods to conduct 2D and 3D simulations for the binary and multicomponent systems. The density inversion theory is proposed based on these researches, and it has been generally accepted.

The freckles formed in VAR ingots are usually distributed along the shape of molten pool^[11,12]. Auburtin et al^[13] proposed an improved Rayleigh number, considering the inclined interface of mushy zone. It is found that the interface of directional solidification is flat, so the formation position of channels is relatively random; while on the inclined interface, the freckles form preferentially at the mid-radius area in VAR ingots. However, this research does not consider the effect of

Received date: December 23, 2021

Foundation item: National Natural Science Foundation of China (51875307)

Corresponding author: Shen Houfa, Ph. D., Professor, Key Laboratory for Advanced Materials Processing Technology, Ministry of Education, School of Materials Science and Engineering, Tsinghua University, Beijing 100084, P. R. China, Tel: 0086-10-62789922, E-mail: shen@tsinghua.edu.cn

Copyright © 2022, Northwest Institute for Nonferrous Metal Research. Published by Science Press. All rights reserved.

alloy elements. Long et al^[14] studied the solidification of superalloys, and reported that the mass of liquid phase is changed with the solidification process proceeding, due to the complexity of the superalloy composition.

The channel segregation with negative density difference, such as A-type segregation in steel ingots^[15], has been widely investigated. However, the positive density difference caused by the channel segregation is rarely reported because of the high experiment cost and the difficulty in in-situ observation of channel formation. Thus, the macrosegregation characteristic in VAR superalloy ingots is rarely studied. The numerical simulation is a suitable research method to solve those problems. Ni et al^[16] firstly developed the conservation equations for the solid and liquid phases through the volume averaging method. The physical exchange terms are solved by the interface equilibrium relationship, so the solid and liquid conservation equations can be used at both macro-scale and micro-scale. In addition, different two-phase models have been constructed based on the solid phases of equiaxed crystal and columnar crystal^[17-19].

In this research, a multicomponent two-phase model was established, and the freckles of IN718 alloy were studied in horizontal directional solidification and VAR processes.

1 Model Establishment

1.1 Experiment

Fig. 1a illustrates the VAR process of ingot with the diameter of 510 mm. The Ni-based IN718 superalloy was remelted, filled into the liquid pool under the consumable electrode, and finally solidified in the mold. VAR process reached the quasi-steady state when the ingot height exceeded a certain value, and the freckles might form.

The horizontal directional solidification was conducted^[14], as shown in Fig. 1b. The dimension of rectangular cavity is 220 mm×140 mm. The cavity was regarded as an extracted part from the ingot, and the boundary conditions were close to the internal environment of VAR process. To form an inclined temperature gradient, the boundaries of thermal convection with different heat transfer coefficients were applied to the bottom and one side wall of cavity. The higher temperature was applied to the cavity bottom, so the heat transfer conditions were similar to the conditions of mushy zone. The adiabatic boundary conditions were applied to the top and the other side wall of cavity.

Fig. 1c shows the geometric model and boundary conditions of VAR system. The axisymmetric VAR model focuses on the molten pool profile after operations with different conditions. The filling process of molten metal was taken into consideration by the dynamic mesh method. The constant heat flux was set as the input thermal boundary condition at the ingot top and a constant convection coefficient was adopted at the ingot bottom. The heat transfer coefficient varying with height and time was applied to the side wall of cavity. The chemical composition of IN718 superalloy is listed in Table 1^[14].

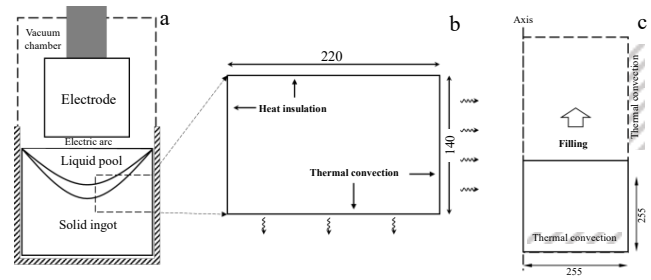


Fig.1 Schematic diagrams of VAR process (a) and horizontal directional solidification (b); geometric model of VAR system (c)

Table 1 Chemical composition of IN718 superalloy (wt%)^[14]

Fe	Cr	Al	Ti	Nb	Mo	C	B	Ni
18.5	19.0	0.5	0.9	5.1	3.0	0.04	0.002	Bal.

1.2 Governing equation

A multicomponent two-phase model was established to investigate the physical transportation between solid and liquid phases in the mushy region. For the VAR process of industrial-size ingots, the grain structure is mainly composed of columnar crystals^[20,21]. Therefore, the columnar crystal-liquid model was selected. The phase fraction of liquid and columnar crystal phases is denoted as f_l and f_c , respectively, and $f_l + f_c = 1$. The related symbols for formula establishment are listed in Table 2. The conservation equations of mass, momentum, energy, and species for both phases were established with the consideration of microscopic phenomena, as follows:

$$\frac{\partial}{\partial t} (f_l \rho_l) + \nabla (f_l \rho_l \mathbf{u}_l) = -\Gamma_{cl} \quad (1)$$

$$\frac{\partial}{\partial t} (f_c \rho_c) = \Gamma_{lc} \quad (2)$$

$$\frac{\partial}{\partial t} (f_l \rho_l h_l) + \nabla (f_l \rho_l h_l \mathbf{u}_l) = \nabla (f_l \rho_l k_l \nabla T_l) - Q_l^* \Gamma_{cl} \quad (3)$$

$$\frac{\partial}{\partial t} (f_c \rho_c h_c) = \nabla (f_c \rho_c k_c \nabla T_c) + Q_c^* \Gamma_{lc} \quad (4)$$

where the subscript c indicates the columnar phase; the subscript l indicates the liquid phase; Γ_{cl} indicates the phase transfer rate from columnar phase to liquid phase during the melting process; Γ_{lc} indicates the phase transfer rate from liquid phase to columnar phase during the solidification process. The columnar crystal phase is assumed to be solidified from the cooling wall to form the bulk and it is static after the bulk formation. Thus, the velocity term in Eq. (2) is omitted. The same assumption is made for the momentum equation, as follows:

$$\frac{\partial}{\partial t} (f_l \rho_l \mathbf{u}_l) + \nabla (f_l \rho_l \mathbf{u}_l \cdot \mathbf{u}_l) = -f_l \nabla p + \nabla (\mu_l f_l \nabla \mathbf{u}_l) + f_l \rho^b \mathbf{g} + K_{lc} (\mathbf{u}_c - \mathbf{u}_l) \quad (5)$$

The growth rate v_R of solid dendrite is part of phase transfer rate Γ_{lc} , and it was modified with coefficient δ , as follows:

Table 2 Nomenclatures of related symbols in formula establishment

Symbol	Meaning
ρ	Density
t	Time
k_l	Thermal conductivity of liquid phase
k_c	Thermal conductivity of columnar crystal
T_l	Temperature of liquid phase
T_c	Temperature of columnar crystal
\mathbf{u}_l	Phase velocity of liquid phase
\mathbf{u}_c	Phase velocity of columnar crystal
h_l	Enthalpy of liquid phase
h_c	Enthalpy of columnar crystal
Q_l^*	Interfacial enthalpy flux of liquid phase
Q_c^*	Interfacial enthalpy flux of columnar crystal
p	Pressure
\mathbf{g}	Gravity
ρ^b	Approximate density
ρ_{ref}	Reference density
K_{lc}	Drag force
D_l	Diffusion coefficient of liquid phase
D_c	Diffusion coefficient of columnar crystal
C_D	Drag coefficient
R_s	Radius of columnar crystal
d_s	Diameter of columnar crystal
$C_{l,i}$	Solute composition of liquid phase
$C_{c,i}$	Solute composition of columnar crystal
$C_{l,i}^*$	Interfacial solute composition of liquid phase
$C_{c,i}^*$	Interfacial solute composition of columnar crystal
β_T	Temperature expansion coefficient
$\beta_{c,i}$	Solute expansion coefficient
T_{ref}	Reference temperature
C_{ref}	Reference solute composition
x_i	Molar fraction
A	Atomic weight
V	Molar volume
H	Reference height of mushy zone

$$v_R = \frac{D_l}{R_s} \left(\frac{C_{l,i}^* - C_{l,i}}{C_{l,i}^* - C_{c,i}^*} \right) \delta \quad (6)$$

The drag force K_{lc} between liquid and solid phases is defined by Eq.(7), as follows:

$$K_{lc} = \frac{3}{4} C_D \frac{f_c f_l \rho_l |\mathbf{u}_c - \mathbf{u}_l|}{d_s} f_1^{-2.65} \quad (7)$$

The multicomponent calculation was introduced into the solute conservation equation and the species transfer process of each element was established through the phase diagrams.

$$\frac{\partial}{\partial t} (f_l \rho_l C_{l,i}) + \nabla \cdot (f_l \rho_l C_{l,i} \mathbf{u}_l) = \nabla \cdot (f_l \rho_l D_l \nabla C_{l,i}) - C_{l,i}^* \Gamma_{cl} \quad (8)$$

$$\frac{\partial}{\partial t} (f_c \rho_c C_{c,i}) = \nabla \cdot (f_c \rho_c D_c \nabla C_{c,i}) + C_{c,i}^* \Gamma_{cl} \quad (9)$$

The Boussinesq approximation with multicomponent calculation was adopted to express the density.

$$\rho^b = \rho_{\text{ref}} [1 - \beta_T (T_l - T_{\text{ref}}) - \sum_i \beta_{c,i} (C_{l,i} - C_{\text{ref}})] \quad (10)$$

The physical properties of IN718 superalloy were calculated by the thermodynamic software JmatPro, and the relative density $\Delta\rho$ of the liquid phase was further calculated by Eq.(11), as follows:

$$\rho = \frac{\sum_i x_i A_i}{\sum_i x_i V_i + \Delta V^M} \quad (11)$$

$$\Delta\rho = \frac{\rho - \rho_l}{\rho_l}$$

where i indicates the element with specific content; ΔV^M is the mixing molar volume^[22]. A modified Rayleigh number was formulated to analyze the formation position of freckles, including the relative density, permeability in mushy zone with the drag force K_{cl} , and the vertical height of the mushy zone as the characteristic length. Besides, the inclination angle of the molten pool profile was also introduced to investigate the influence of temperature gradient θ and gravity direction angle α .

$$Ra_{\text{modified}} = \frac{\Delta\rho (f_l) \mathbf{g} K_{lc} H}{\mu V_R} \sin(\theta - \alpha) \cos\theta \quad (12)$$

1.3 Geometric model

In VAR process, the molten metal dropped into the water-cooled copper mold and solidified into a new ingot. The dynamic mesh algorithm was applied to the governing equations to calculate the filling process of the liquid metal during VAR process. The time derivative terms were discretized by the first-order backward difference method. The integral form of the conservation equation for the general scalar φ on the arbitrary control volume V can be expressed by Eq.(13), as follows:

$$\frac{\partial}{\partial t} \int_V \rho \varphi dV + \int_{\partial V} \rho \varphi (\mathbf{u} - \mathbf{u}_g) \cdot d\mathbf{A} = \int_{\partial V} \Gamma \nabla \varphi \cdot d\mathbf{A} + \int_V S_\varphi dV \quad (13)$$

where ρ is the fluid density, \mathbf{u} is the flow velocity vector, \mathbf{u}_g is the velocity of moving mesh, Γ is the diffusion coefficient, S_φ is the source term of φ .

The simulations were performed under a volume-averaged frame with semi-implicit method for pressure linked equation (SIMPLE) algorithm. The related material parameters are listed in Table 3.

2 Results and Discussion

The local thermodynamic equilibrium was used to calculate the connection between liquid composition and temperature/solid fraction during solidification. The fluctuation of element composition and liquid density difference with solid phase fraction of IN718 superalloy is shown in Fig.2. Nb is a major segregation element in IN718 superalloy, resulting in the positive density differences (Fig. 2b). According to the thermodynamic data, the liquid density of IN718 superalloy is steadily increased with the solidification proceeding, indicating that the Nb component undergoes the interdendritic positive segregation.

Table 3 Material parameters of IN718 superalloy

Parameter	Value
Density, $\rho/\text{kg}\cdot\text{m}^{-3}$	7491
Melting temperature of Ni, T_m/K	1728
Liquidus temperature, T_{liq}/K	1609
Solidus temperature, T_{sol}/K	1533
Latent heat, $L/\text{J}\cdot\text{kg}^{-1}$	2.72×10^5
Specific heat, $c_p/\text{J}\cdot\text{kg}^{-1}\cdot\text{K}^{-1}$	620
Thermal conductivity, $k/\text{W}\cdot\text{m}^{-1}\cdot\text{K}^{-1}$	25
Liquid viscosity, $\mu_l/\text{kg}\cdot\text{m}^{-1}\cdot\text{s}^{-1}$	1×10^{-3}
Liquid solute diffusion coefficient, $D_l/\text{m}^2\cdot\text{s}^{-1}$	1.0×10^{-8}
Solid solute diffusion coefficient, $D_s/\text{m}^2\cdot\text{s}^{-1}$	3.0×10^{-12}
Initial temperature, T_0/K	1800
Thermal expansion coefficient, β_T/K^{-1}	1.2×10^{-5}
Solute expansion coefficient, $\beta_{c,i}/\text{wt}\%^{-1}$	-0.2
Primary dendrite arm spacing, λ_1/m	1.3×10^{-3}
Initial concentration of Nb, $C_{0,\text{Nb}}/\text{wt}\%$	5.1
Initial concentration of Ti, $C_{0,\text{Ti}}/\text{wt}\%$	0.9
Liquidus slope of Nb, $m_{\text{L,Nb}}/\text{K}\cdot\text{wt}\%^{-1}$	-1090.0
Liquidus slope of Ti, $m_{\text{L,Ti}}/\text{K}\cdot\text{wt}\%^{-1}$	-1102.0
Solute partition coefficient of Nb, $k_{\text{p,Nb}}$	0.48
Solute partition coefficient of Ti, $k_{\text{p,Ti}}$	0.91

2.1 Horizontal directional solidification

The transportation and macrosegregation of components during the horizontal directional solidification of IN718 superalloy in the rectangular cavity with dimension of 220 mm×140 mm (Fig. 1b) were simulated. Fig. 3 shows the fluid flow after solidification for 300 and 500 s. The mushy zones are indicated by the dashed lines in Fig. 3a and 3c. It is found that partial mush is remelted, and the channels emerge in the solidified mush and then creep over time. The typical channels are chosen to evaluate the local flow field. The channels grow downward, as indicated by the streamlines and velocity vectors. Furthermore, because the segregation elements are not diffused into the matrix yet, the matrix still exhibits a general flow pattern, which is dominated by the thermosolutal convection. The liquid sinking occurs in the mushy zone and neighboring areas.

Fig. 4 shows the Nb and Ti element distributions in IN718

superalloy ingot after solidification for 700 s. Because the density of Nb and Ti segregation elements is quite different (Nb is much heavier than Ti), the density difference in liquid displays the opposite changing patterns. Thus, the solidification of Nb and Ti elements in IN718 superalloy was investigated for macrosegregation analysis. Both Nb and Ti elements are positive segregation elements with distinct diffusion coefficients, and they are enriched along the propagation channels in mushy zone, as indicated by the liquid fraction isolines of 0.05 and 0.95 (the dashed lines) in Fig. 4.

The simulated channel and freckle formation mechanism were analyzed and compared with the experiment results^[14], as shown in Fig. 5. The direction of the temperature gradient and the liquid density difference affect the formation and development of freckles when the molten pool profile has an inclination angle. It can be seen that the simulated morphology of channels agrees well with the experiment one, demonstrating the reliability of this numerical model. The channel generation on the arc-shaped solidification interface with positive density difference is illustrated in Fig. 6. The main influence factors for the fluid flow are the thermal gradient G_T and liquid density difference $\Delta\rho$. The thermal gradient determines the moving direction of molten pool profile and allows the liquid flowing along the solid-liquid interface. Partial mush is corroded and remelted because of the decreasing liquidus induced by the increasing element content, and the interdendritic channels open up. Finally, the enriched solutes are solidified in the channels with decreasing the temperature, and the freckles appear in the ingot.

Table 4 presents the simulated element contents at the typical freckle position after solidification (point A in Fig. 5a), and the experiment results from Ref. [23] are also listed for comparison. It is found that both Nb and Ti are positively segregated, and the simulated results are close to the experiment measurements.

2.2 Vacuum arc remelting

2.2.1 Solidification process

The molten pool profile of IN718 superalloy ingot with melting rate of 0.083 kg/s is obtained by simulation and compared with the results in Ref. [24], in order to adjust and verify the boundary conditions during the filling process, as shown in Fig. 7. The simulated molten pool shape shows good

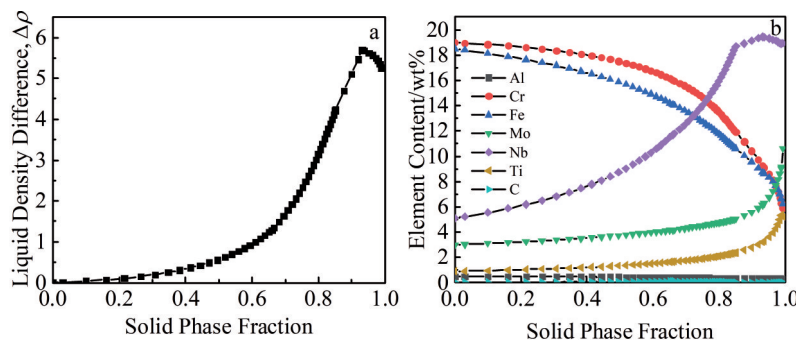


Fig. 2 Relationships of liquid density difference $\Delta\rho$ (a) and element contents (b) with solid phase fraction during solidification of IN718 superalloy

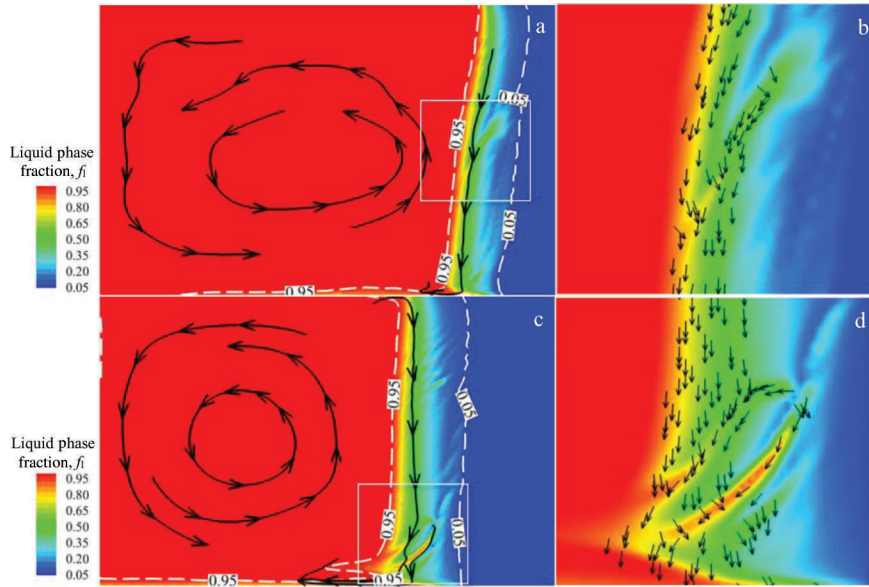


Fig.3 Fluid streamlines (a, c) and local flow vectors (b, d) of IN718 superalloy after horizontal directional solidification for 300 s (a, b) and 500 s (c, d)

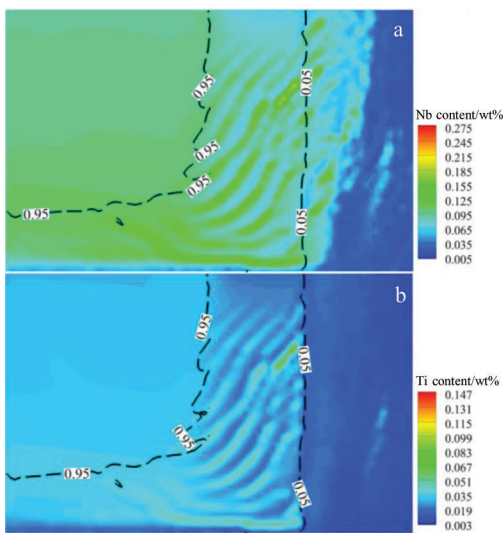


Fig.4 Nb (a) and Ti (b) element distributions in IN718 superalloy after horizontal directional solidification for 700 s

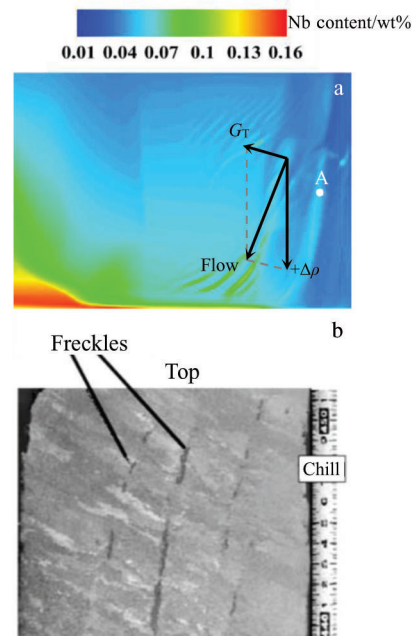


Fig.5 Simulated Nb element distribution after solidification for 1500 s (a); experiment result of freckle formation in IN718 superalloy ingot^[14] (b)

agreement with the experiment one, indicating the accuracy of the prediction model.

Fig. 8 shows the simulated solidification sequence and the macrosegregation of IN718 superalloy ingot with melting rate of 0.409 kg/s. The channel segregation appears in the mushy zone, and the convection pattern is verified by the streamlines, as shown in the left sides of Fig. 8b~8d. The molten pool is deepened with the filling process and it reaches the quasi-steady state after solidification for 2000 s. Most channels are densely distributed near the ingot bottom as a result of unstable stage during the early solidification, as shown in Fig. 8b and 8c. The dashed lines in the right parts of Fig. 8 indicate the molten pool profiles. With the ingot solidification proceeding, the number of channels formed in mushy zone

becomes less and less, because it is more and more difficult for the liquid phase to flow into the mushy zone. In addition, the formation conditions of the channel are hard to achieve. Basically, Fig. 8 shows the characteristics of regional macrosegregation.

Fig. 9 presents the Nb element distribution comparison between the simulated local freckles (zone I in Fig. 8d) and the measured Nb element distribution^[25]. Since a few relevant process parameters are available, only the growing trend and

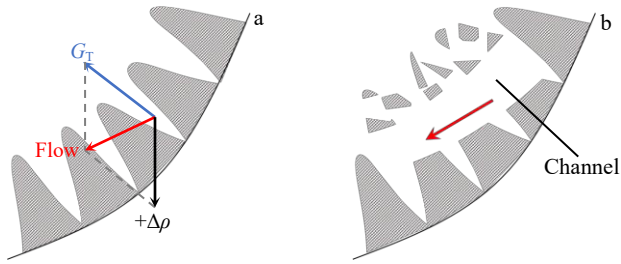


Fig.6 Schematic diagrams of formation mechanism of channels (a) and freckles (b) with positive density difference in liquid

Table 4 Simulated and experimental results of Nb and Ti contents in freckle area (wt%)

Segregation element	Experiment	Simulation
Nb	9.43	10.10
Ti	1.33	1.24

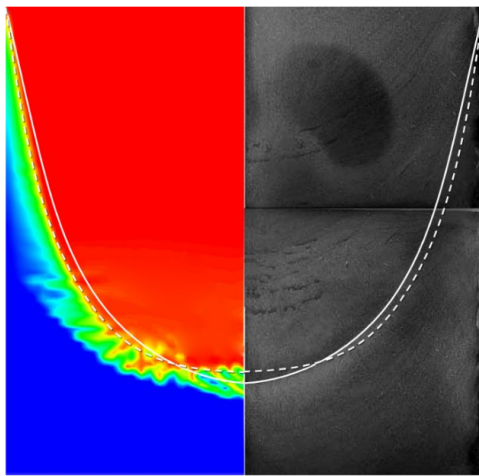


Fig.7 Comparison between simulated and experiment molten pool profiles of IN718 superalloy ingot with melting rate of 0.083 kg/s (the dashed line indicates the calculated molten pool shape; the solid line indicates experimental molten pool shape)

the solute composition of freckles in the region of 100 mm×100 mm (zone I) are compared. It can be seen that the simulated results show good agreement with the experiment

ones.

It is estimated that the channel formation depends on the strength of thermosolutal convection. The modified Rayleigh number ($Ra_{modified}$) along the radius in mushy zone is applied to predict the channel tendency, as shown in Fig.10. The freckles in VAR ingots often appear around the mid-radius area. The maximum value of $Ra_{modified}$ occurs at about 0.2 m from the center of IN718 superalloy ingot with the melting rate of 0.409 kg/s, which is basically consistent with the channel distribution area in the simulation results (Fig. 8d). The deviation exists because the filling rate used in the calculation is larger than that in the experiments, resulting in the deeper molten pool and smaller distance from molten pool to the vertical direction.

2.2.2 Melting rate

According to Fig.6, the development of channel segregation is affected by the inclination of the molten pool profile, which can be adjusted by the process parameters of electrode melting rate. The faster the melting rate, the deeper the molten pool and the more the vertical sidewalls of the molten pool. Three electrode melting rates of 0.306, 0.409, and 0.765 kg/s were used for simulation. The solidification and macrosegregation with different melting rates after solidification for 2000 s are compared, as shown in Fig. 11. The reason for choosing the same solidification time instead of the same height for comparison is that the solidification state at the same time is more similar and more comparable during the filling simulation process with the dynamic mesh.

When the cooling conditions are fixed, the slower the solidification, the longer the duration for the channel formation and development (Fig. 11). As a result, the number of channels is increased and the distribution region is wider. When the melting rate is 0.306 kg/s, only a few freckles appear near the mid-radius area and are distributed chaotically with different depths and widths. When the melting rate is 0.765 kg/s, there are plenty of freckles arranging neatly along the side wall of the molten pool. Moreover, the growth direction of the channels also shows a certain regularity. With increasing the melting rate, the angle between the channel and gravity direction becomes smaller ($\theta_1 > \theta_2 > \theta_3$), as shown in Fig. 11. Fig. 12 presents the solute distributions at the ingot height of 300 mm with different melting rates. It is obvious

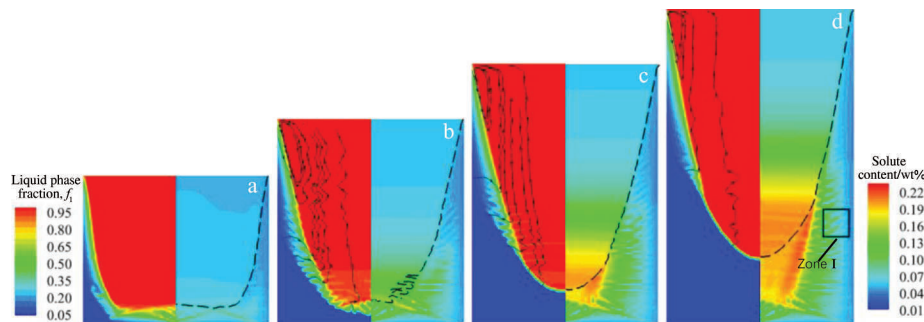


Fig.8 Solidification sequence of IN718 superalloy ingot with melting rate of 0.409 kg/s after solidification for 500 s (a), 1000 s (b), 1500 s (c), and 2000 s (d)

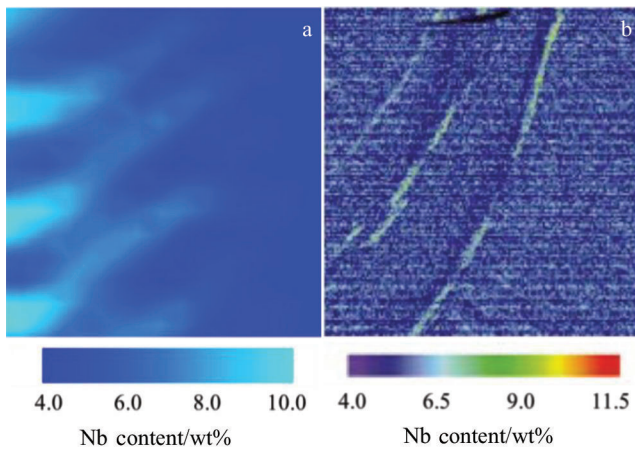


Fig.9 Nb element distributions of simulated (a) and experimental (b) freckles in IN718 superalloy ingots

that the segregation degree with larger melting rate is higher. In the area close to the side wall of ingots, the solute composition is oscillated due to the channel formation.

2.2.3 Cooling rate

The cooling conditions can also affect the molten pool

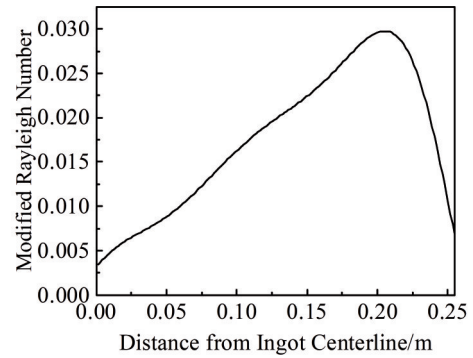


Fig.10 Modified Rayleigh number in mushy zone along radius direction of IN718 superalloy ingot with melting rate of 0.409 kg/s

shape. Different heat transfer coefficients (H_1 and H_2 with $H_2=2H_1$) are applied with fixed calculation parameters. Fig. 13 presents the solidification and macrosegregation of IN718 ingots with different cooling rates. With the heat transfer coefficient H_2 , the solidification reaches the quasi-stable state earlier at around 1500 s than that with H_1 does. The heat

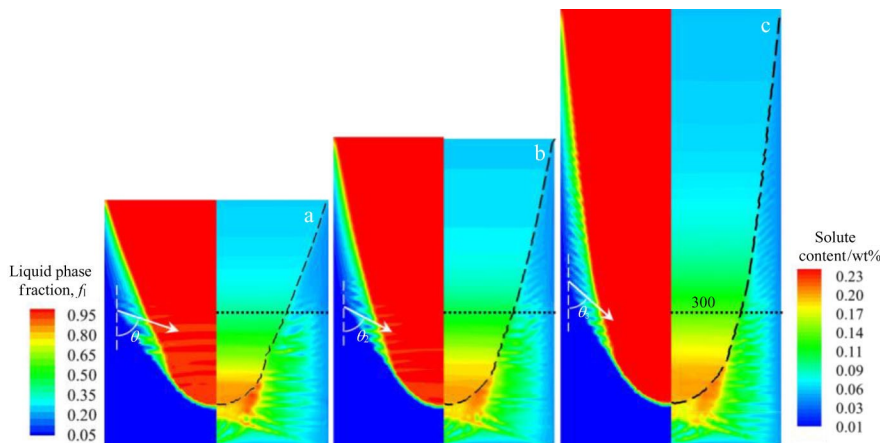


Fig.11 Solidification states of IN718 superalloy ingots after solidification for 2000 s with different melting rates: (a) 0.306 kg/s, (b) 0.409 kg/s, and (c) 0.765 kg/s

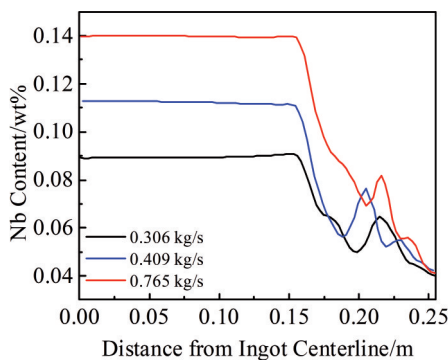


Fig.12 Nb contents at height of 300 mm of IN718 superalloy ingot with different melting rates after solidification for 2000 s

transfer coefficient, i.e., the cooling rate has slight influence on the number of freckles, but it significantly changes the growing direction of freckles.

The fast cooling process results in the shallow molten pool, therefore leading to the large angle between the molten pool profile and the gravity direction ($\alpha_2 > \alpha_1$). The typical channels are marked by the dashed lines in Fig. 13. The inclination of the channel changes ($\theta_2 > \theta_1$). Before the solidification reaches the quasi-stable stage, the shape of the molten pool changes gradually with the filling process proceeding, as shown in Fig. 8. It can be observed that the angle between the channel and the gravity direction gradually decreases from the bottom to the top of the molten pool profile.

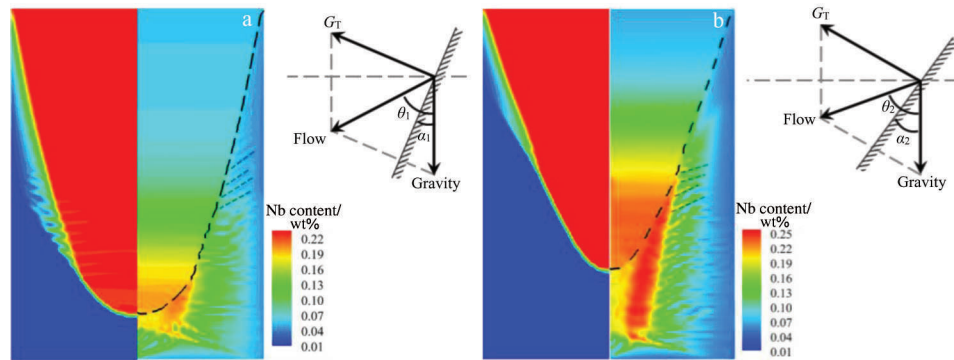


Fig.13 Solidification states of IN718 superalloy ingots after solidification for 1500 s with melting rate of 0.409 kg/s and heat transfer coefficient of H_1 (a) and H_2 (b)

3 Conclusions

1) A multicomponent two-phase model was established to simulate the solidification of IN718 superalloy during vacuum arc remelting (VAR) process. The model including the columnar crystal phase and liquid phase describes the solid-liquid interaction coupling macro-transportation and micro-flux at solidification front with thermodynamics.

2) The segregation elements in IN718 superalloy ingot contribute to the positive density difference, therefore leading to the downward interdendritic flow.

3) The freckles tend to develop at the early solidification stage. The high melting rate can achieve the deep molten pool and promote the freckle formation, which causes the serious macrosegregation. The fast cooling process can reach the stable solidification early but results in the large macrosegregation. Both melting rate and cooling rate have apparent influence on the growing direction and formation position of freckles.

References

- Chatterjee M, Patra A, Babu R R. *Aerospace Materials and Material Technologies*[M]. Singapore: Springer, 2017: 3
- Zhang Yong, Li Xinxu, Wei Kang et al. *Acta Metallurgica Sinica* [J], 2020, 56(8): 1123
- Du Jinhui, Lv Xudong, Dong Jianxin et al. *Acta Metallurgica Sinica*[J], 2019, 55(9): 1115
- Zhang Bei Jiang, Huang Shuo, Zhang Wenyun et al. *Acta Metallurgica Sinica*[J], 2019, 55(9): 1095 (in Chinese)
- Dong Jianxin, Zhang Maicang, Zeng Yanping et al. *Rare Metal Materials and Engineering*[J], 2006, 35(2): 176 (in Chinese)
- Copley S M, Giamei A F, Johnson S M et al. *Metallurgical and Materials Transactions B*[J], 1970, 1(12): 3455
- Sarazin J R, Hellawell A. *Metallurgical Transactions A*[J], 1988, 19(7): 1861
- Sample A K, Hellawell A. *Metallurgical and Materials Transactions A*[J], 1984, 15(12): 2163
- Felicelli S D, Heinrich J C, Poirier D R. *Journal of Crystal Growth*[J], 1998, 191(4): 879
- Felicelli S D, Poirier D R, Heinrich J C. *Metallurgical and Materials Transactions B*[J], 1998, 29(4): 847
- Wang Ling, Dong Jianxin. *Ordnance Material Science and Engineering*[J], 2006, 29(4): 59 (in Chinese)
- Dong Jianxin, Zhang Maichuang, Zeng Yanping. *Ordnance Material Science and Engineering*[J], 2005, 28(1): 1 (in Chinese)
- Auburtin P, Wang T, Cockcroft S L et al. *Metallurgical and Materials Transactions B*[J], 2000, 31(4): 801
- Long Z D, Liu X B, Yang W H et al. *Materials Science and Engineering A*[J], 2004, 386(1-2): 254
- Cao Y F, Chen Y, Li D Z. *Acta Materialia*[J], 2016, 107: 325
- Ni J, Beckermann C. *Metallurgical and Materials Transactions B* [J], 1991, 22(3): 349
- Li J, Wu M, Hao J et al. *Computational Materials Science*[J], 2012, 55: 419
- Li J, Wu M, Hao J et al. *Computational Materials Science*[J], 2012, 55: 407
- Ludwig A, Gruber-Pretzler M, Wu M H et al. *Fluid Dynamics and Materials Processing*[J], 2005, 1(4): 285
- Sankar M, Prasad S V V, Baligidad R G et al. *International Journal of Refractory Metals and Hard Materials*[J], 2015, 50: 120
- Jardy A, Ablitzer D. *Materials Science and Technology*[J], 2009, 25(2): 163
- Sung P K, Poirier D R. *Metallurgical and Materials Transactions A*[J], 1999, 30(8): 2173
- Pollock T M, Tin S. *Journal of Propulsion and Power*[J], 2006, 22(2): 361
- Wang X H, Ward R M, Jacobs M H et al. *Metallurgical and Materials Transactions A*[J], 2008, 39(12): 2981
- Van Den Avyle J A, Brooks J A, Powell A C. *JOM*[J], 1998, 50(3): 22

IN718 高温合金水平定向凝固和真空电弧重熔过程中 “黑斑”形成的多组元数值模拟

李 桐, 沈厚发

(清华大学 材料学院, 北京 100084)

摘 要: 建立了多组元两相模型来描述 IN718 高温合金凝固过程中的宏观/微观传输和“黑斑”形成, 并应用动态网格算法模拟真空电弧重熔 (VAR) 过程中的填充过程。首先, 使用热力学计算方法求解液相成分随固相分数的变化, 并获得多组元合金的枝晶间液相密度。之后模拟了水平定向凝固工艺下形成的“黑斑”, 并与实验结果进行对比, 研究其形成机理和影响因素。最后, 利用所开发的模型来研究工艺参数对工业规模 VAR 铸锭中“黑斑”的影响。结果表明, 元素组成对凝固过程中液相的密度变化有显著影响, “黑斑”的形成伴随着高热溶质对流强度。“黑斑”的生长方向由液相密度差和凝固界面相对重力方向的角度决定。在 VAR 过程中, 熔池形状受电极熔化速率和冷却速率影响。

关键词: 黑斑; 宏观偏析; 数值模拟; 高温合金; 真空电弧重熔

作者简介: 李 桐, 女, 1997年生, 硕士, 清华大学材料学院, 北京 100084, E-mail: lit19@mails.tsinghua.edu.cn